Journal of Materials Chemistry A

PAPER

View Article Online
View Journal | View Issue

Cite this: J. Mater. Chem. A, 2017, 5, 23720

Rapidly annealed nanoporous graphene materials for electrochemical energy storage

Hao Yang,[a] Santhakumar Kannappan,[b] Amaresh S. Pandian,[c] Jae-Hyung Jang,[b] Yun Sung Lee[c] and Wu Lu*[ab]

Received 1st September 2017
Accepted 5th October 2017

DOI: 10.1039/c7ta07733e

rsc.li/materials-a

The urgent need for efficient energy storage devices greatly stimulates the development of high power, highly efficient, environmentally friendly, and low-cost energy storage devices. Supercapacitors, unlike batteries, store energy by ion adsorptions on high surface area electrodes. The physical ion migration provides a high charging/discharging rate, power density, and reversibility. In this work, we synthesize graphene materials by a rapid thermal annealing process and examine the material properties. With the synthesized graphene as electrodes, the outstanding electrochemical performance of these supercapacitors is demonstrated. This provides a new method for developing supercapacitors with high charge/energy storage capability at low cost.

1. Introduction

A critical challenge that people encounter in the 21st century is how to ensure future energy security. With the development of various sustainable energy sources, an efficient energy storage device with higher energy storage capabilities is needed. A supercapacitor, or electrochemical capacitor, stores electrical charges in an electric double layer (EDL) at the interface between the electrode and electrolyte. Due to the high surface area and small EDL separation, the specific capacitances of supercapacitors are expected to be higher than conventional capacitors.[1–3] The ion migration in the EDL is much faster and more reversible than the redox reaction in batteries resulting in the ultra-high power density and cycling stability. The EDL theory was first demonstrated in the late 1800s, but the first supercapacitor device was not developed until 1957 by H. I. Becker.[4]

In the past decade, supercapacitors attracted a lot of attention due to the breakthrough in porous electrode materials, such as carbon materials and metal oxides. Among all the carbon materials, graphene is the ideal electrode candidate, due to its high surface area, mechanical strength, chemical stability, and electrical conductivity.[6–17] With these superior properties, there have been a lot of efforts to exploit graphene in many applications, such as transparent electrodes, hydrogen storage, water desalination, and thermal management applications.[18–21] Nanoporous graphene materials have been studied in supercapacitors, showing great improvement in the electron conductivity, energy density, power density and cycling stability.[22–28] The mechanical and chemical vapor deposition methods can produce high quality graphene, but the high cost and planar structure exclude it from electrochemical energy storage applications. Because of graphene's strong tendency to agglomerate and its hydrophobic nature, it's quite challenging to produce graphene directly from graphite. Alternatively, graphene can be synthesized on a large scale at low cost by reducing and exfoliating graphite oxide (GO).[29–31] Several reduction and exfoliation methods have been developed, such as chemical reduction,[22,23] microwave irradiation,[24] thermal annealing,[5,25,26] powerful sonication,[27] laser scribing,[28] and so on. In contrast to other methods, thermal annealing provides few layer graphene with less agglomeration, higher surface area, better electric conductivity, and higher yield.[32,33] Previously, the thermal annealing was investigated to exfoliate and reduce GO at high temperature above 1000 °C in an inert gas environment.[25,34,35] Bing Zhao *et al.* reported the exfoliation of GO at temperatures varying from 150 to 900 °C and a slow heating rate of 5 °C min^{-1}.[36] Both the surface area and the electric conductivity decrease with increasing the temperature above 500 °C, which results from the coalescence of graphene sheets during the slow heating process. In addition, the slowly heated sample exhibits high defect content. To improve the material quality of thermally annealed graphene and thus the energy storage performance, we annealed the GO at 500 °C at a high heating rate around 70–80 °C s^{-1} in argon. The surface area, reduction degree, pore size distribution, and morphology are characterized and discussed. With these rapidly annealed graphene (RAG) electrodes, a specific capacitance of 279 F g^{-1} and an energy density of 135 W h kg^{-1} are achieved.

[a]Department of Electrical and Computer Engineering, The Ohio State University, Columbus, Ohio 43210, USA. E-mail: lu.173@osu.edu

[b]Department of Nanobio Materials and Electronics, Gwangju Institute of Science and Technology, Gwangju 500-712, Republic of Korea

[c]Faculty of Applied Chemical Engineering, Chonnam National University, Gwangju 500-757, Republic of Korea

2. Experimental

2.1 Preparation of graphite oxide

GO was produced by modified Hummer's method,[37] which has been reported in our earlier work.[5] In short, graphite powder was oxidized with $K_2S_2O_8$ and P_2O_5 in concentrated H_2SO_4. The resultant product was then washed with DI water until the pH value reached neutral. The pre-oxidized graphite was mixed with $KMnO_4$ and H_2SO_4 for further oxidation in an ice bath. To remove metal ions, the solution was rinsed with HCl and dialyzed for two weeks.

2.2 Synthesis of RAG

The process we have developed involves a one step process using rapid annealing in an Ar environment to exfoliate the stacked GO sheets and remove the oxide groups simultaneously. Here, the GO was put in a quartz tube and purged with Ar gas. Then the temperature was ramped to 500 °C at the heating rate around 70–80 °C s^{-1}. The evolved gases such as water vapor and CO_2 cause a rapid expansion inside the stacked layers, shown in Fig. 1a. The process can be visually observed with the rapid volume expansion. In this work, we show that the GO is effectively reduced and exfoliated indicated by the electron microscopy images and material characterization data. The synthesized material was characterized by a series of material characterization methods, including FESEM, TEM, XRD, Raman, XPS, FTIR and TGA. The surface area and pore size distribution were analyzed with nitrogen isotherm adsorption measurements.

2.3 Electrochemical measurements

The electrode preparation process and cell structure are the same as what we have reported before.[5] The assembled cell was characterized with cyclic voltammetry (CV), electrochemical impedance spectroscopy (EIS), and galvanostatic charge/discharge (GCD). The instruments used are CH Instruments CHI760D, Zahner Electrochemical Unit 1M6e, and Nagano BTS-2004H.

3. Results and discussion

3.1 Material characterization

The SEM image (Fig. 1b) shows the morphology of the exfoliated graphene material synthesized by rapid annealing with a "comb-like" network. The relatively large inter sheet spacing as well as comb network suggests the effectiveness of rapid thermal exfoliation and leads to a better utilization of the surface area buried beneath the electrode surface. The TEM image (Fig. 1c) further clearly indicates that the rapid annealing process can effectively exfoliate the GO. It shows the single layer or few layer RAG flake with very limited agglomeration. The selected-area electron diffraction (SAED) pattern in the inset of Fig. 1c shows clear hexagonal diffraction dots demonstrating that the RAG had been restored to the hexagonal graphene

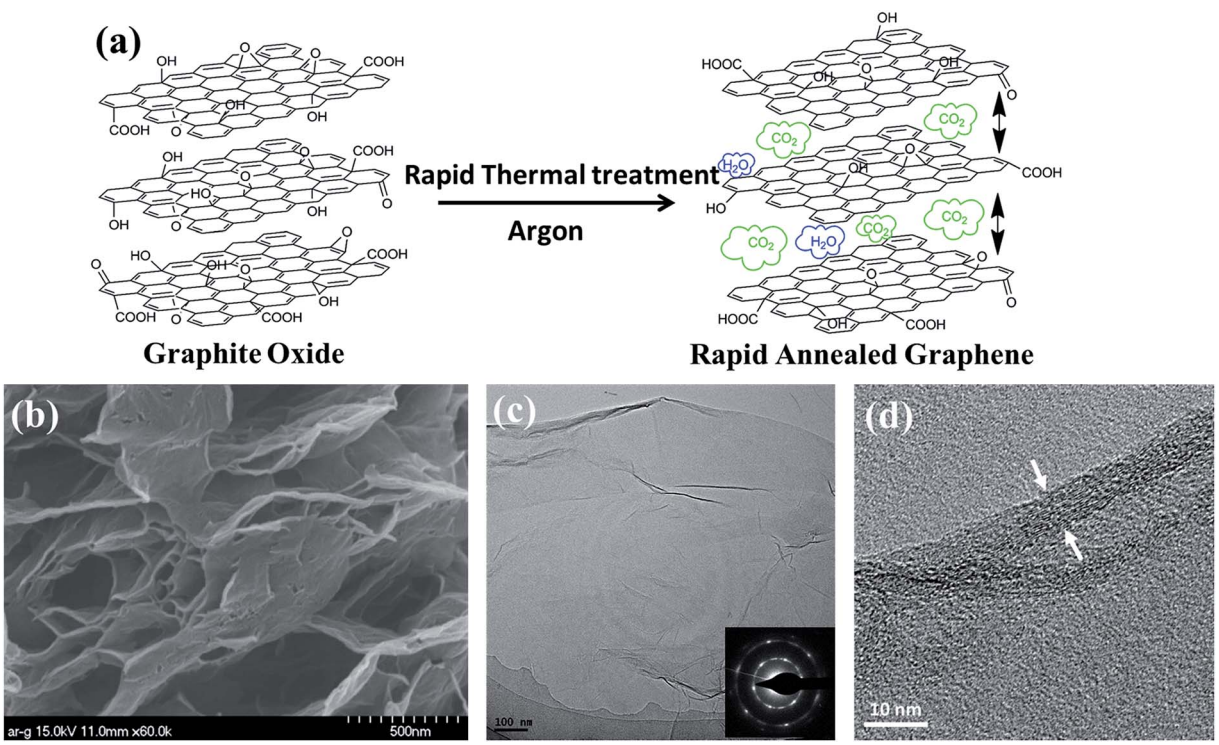

Fig. 1 (a) Schematic demonstrating the process of one step exfoliation and reduction process of GO with rapid thermal annealing. (b) A SEM image of a RAG sheet. It reveals the typical morphology of these graphene materials. (c) TEM image of the RAG material. The inset shows a clear hexagonal electron diffraction pattern. (d) A higher resolution TEM image of the edge of a RAG sample. The arrows point to the edge of RAG showing multilayer stacking.

framework. The high resolution TEM image in Fig. 1d shows the fringe structure of the RAG with around 15 layers of graphene stacked together in this sample.

Fig. 2a shows the XRD patterns of the GO and RAG materials. As is known, the (002) peak of graphite is around 26° with a corresponding interlayer spacing of 3.33–3.35 Å.[38–40] The as-prepared GO shows an intense 2θ peak around 12.06° and an increased interlayer spacing of 7.52 Å due to the insertion of oxygen groups. With the rapid thermal treatment, the removal of oxygen groups in GO leads to the peak shifting to 25.20° and a decrease of interlayer spacing to 3.53 Å in the RAG materials. The (002) peak and the interlayer spacing of RAG are closer to those of the graphite, suggesting that RAG is fully reduced.

Because of the amorphization during the oxidation process, there are a certain amount of sp^3 bonded carbons in the GO sheets.[41] As a result, a broad and relatively intense D band is commonly observed around 1350 cm^{-1} as well as a broad G band in the Raman spectrum.[42] During the transition from graphite to GO, it generates some defects or vacancies,[25,34,42–44] resulting in an I_D/I_G ratio of 0.91. In the case of RAG, the I_D/I_G ratio is 0.93, which is smaller than the value reported for slowly annealed graphene.[36] Compared with GO, the intensity ratio I_D/I_G of RAG increases very limitedly, suggesting that the rapid thermal treatment didn't introduce many defects. In RAG, the G band shifts to the higher frequency region compared with graphite. This blue shift of the G band could be caused by the presence of double bonds which resonate at high frequencies,[42] the merge of the defects induced the D′ band at 1620 cm^{-1},[45–47] and the unmodified graphitic areas.[48]

The XPS spectra reveal the presence of carbon and oxygen with no other detected hetero elements, shown in the inset of Fig. 2c. The C/O ratio of RAG is as high as 7.9, which compares favorably with graphene materials annealed at a slow heating rate.[36] The slowly annealed graphene shows a C/O ratio of 5.56 at 500 °C. Even the C/O ratio of slowly annealed graphene at 700 °C is comparable with our RAG annealed at lower temperature. In RAG, the main peak attributed to the non-oxygenated carbon locates at 284.6 eV. And the intensity of oxygen-containing groups such as C–OH/C–O–C (286.3 eV), C═O (287.8 eV), and H–O–C═O (288.8 eV) is obviously reduced during the rapid thermal treatment. The C–O–C group has a similar binding energy to C–OH.[49] The FTIR spectrum of RAG (Fig. 2d) shows characteristic peaks at 1719 cm^{-1} (C═O), 1637 cm^{-1} (C═C), and 1385 cm^{-1} (C–O), and the band between 1050 and 1190 cm^{-1} (C–OH).[50–54] The low peak intensity of oxygen related groups indicates a substantial removal of oxide by the rapid annealing. The strong absorption peak at approximately 3437 cm^{-1} is attributed to the

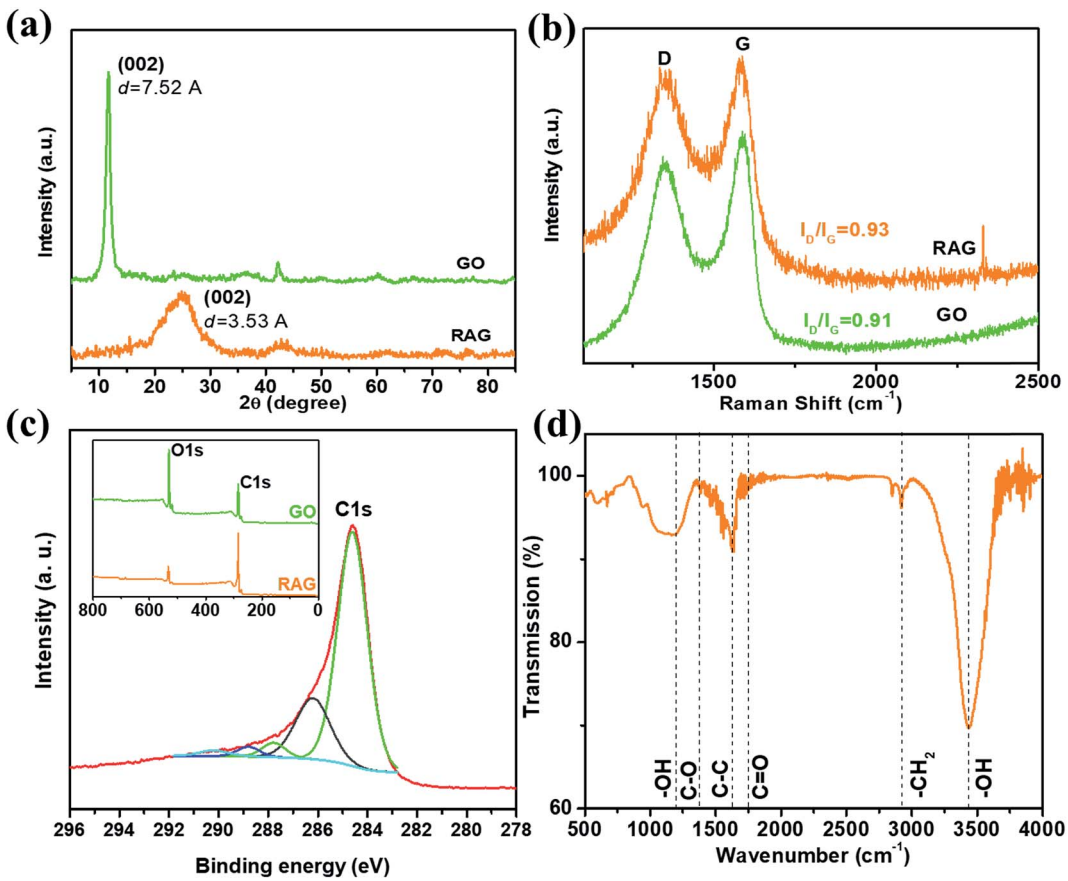

Fig. 2 (a) XRD spectra of GO and RAG samples showing the interlayer spacing decrease after the exfoliation and reduction. (b) Raman spectrum of the RAG sample. (c) XPS C 1s spectrum of the RAG sample and the inset is the comparison between GO and RAG. (d) FTIR spectrum of the RAG powder.

stretching and bending vibrations of OH groups in the water molecules absorbed on RAG, common for porous materials. The two peaks at 2850 and 2918 cm^{-1} correspond to the asymmetric and symmetric stretching vibrations of CH_2.[54]

The N_2 adsorption isotherm measurements can provide information about the surface area and pore size distribution of the material. The N_2 adsorption/desorption of RAG (Fig. 3a) shows a typical type IV isotherm curve with a hysteresis loop at a relatively high pressure associated with capillary condensation. The almost linear region is the stage where the monolayer coverage is completed and the multilayer adsorption is about to start. The type H3 hysteresis loop in the isotherm implies that the graphene plates aggregate forming slit-shaped mesopores.[55] The modern non-local density functional theory (NLDFT) can provide accurate pore prediction in a micropore size range. With NLDFT (Fig. 2c), it is found that the micropores in RAG distribute around 0.78 nm with a pore volume of 0.19 $cm^3\ g^{-1}\ nm^{-1}$. Barrett–Joyner–Halenda (BJH) methods based on the Kelvin equation are widely used for extracting the mesopore size distribution. With BJH methods, the mesopore size is found to distribute in a narrow range of 3.77–4.27 nm with a pore volume of 0.55 $cm^3\ g^{-1}\ nm^{-1}$. Compared with samples annealed at a slower heating rate,[56] the micropore volume is higher and the mesopore volume is slightly smaller. The Brunauer–Emmett–Teller (BET) surface area of RAG is determined to be around 612 $m^2\ g^{-1}$. The BET surface area doesn't necessarily equal the actual accessible sites for accommodating electrolyte ions. Instead, the device performance can only be characterized by CV, GCD and EIS in assembled supercapacitor cells.

The thermal stability of GO and RAG is analyzed by thermogravimetric analysis (TGA), shown in Fig. 4. For the GO sample, the major weight loss occurs between 100 °C and 200 °C, resulted from the pyrolysis of oxygen groups and the release of CO_2.[57] The total weight loss of GO is at 43% at 300 °C and 53% at 500 °C. In contrast, the RAG sample shows better thermal stability than GO. The total weight loss is 0.3% at 300 °C and 6.5% at 500 °C. The thermal stability of RAG is attributed to the absence of oxygen groups. With the weight of CO_2 molecules and the volume of gaps, the pressure of the evolved gas is obtained to be 39.4 MPa at a temperature of 500 °C according to the ideal gas law.[5] Based on Lifshitz's theory, the pressure required to exfoliate the multilayer can be written as

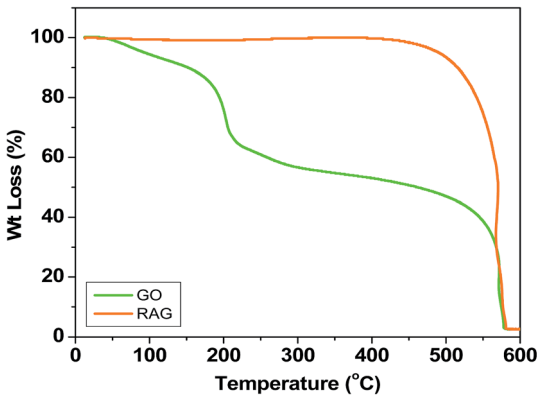

Fig. 4 The thermal gravimetric data for GO and RAG.

$P = \frac{\partial G}{\partial l} = \frac{A_{\mathrm{Ham}}}{6\pi l^3}$, where G is the free energy, A_{Ham} is the Hamaker coefficient and l is the separation between two slabs. As demonstrated in our previous publication, the evaluated Hamaker coefficient for the GO system is approximately 1.76 zJ.[5] The estimated pressure to exfoliate the GO layers is 1.51 MPa.[25,58] This calculated pressure is lower than the estimated gas pressure. This, however, doesn't mean that the high gas pressure is not required. With rapid annealing, the fast expansion of interlayer spacing decreases the gas pressure, leading to lower pressure than estimated. In addition, it would require a much higher pressure to initialize the exfoliation due to the smaller interlayer spacing along the edges and extra capillary forces to overcome.[5]

3.2 Electrochemical measurements

To examine the energy storage performance of RAG electrodes, the graphene supercapacitors were assembled in a symmetrical two-electrode cell using the ionic liquid $EMIMBF_4$ electrolyte. The performance of supercapacitors was evaluated with CV, GCD and EIS measurements. Unlike other electrolytes, $EMIMBF_4$ has a wide potential window up to 4 V as well as a high conductivity,[59] leading to high energy density and low equivalent series resistance (ESR). The CV curves of RAG electrodes at scan rates from 5 mV s^{-1} to 100 mV s^{-1} exhibit no redox peaks, shown in Fig. 5a. It suggests that the device is

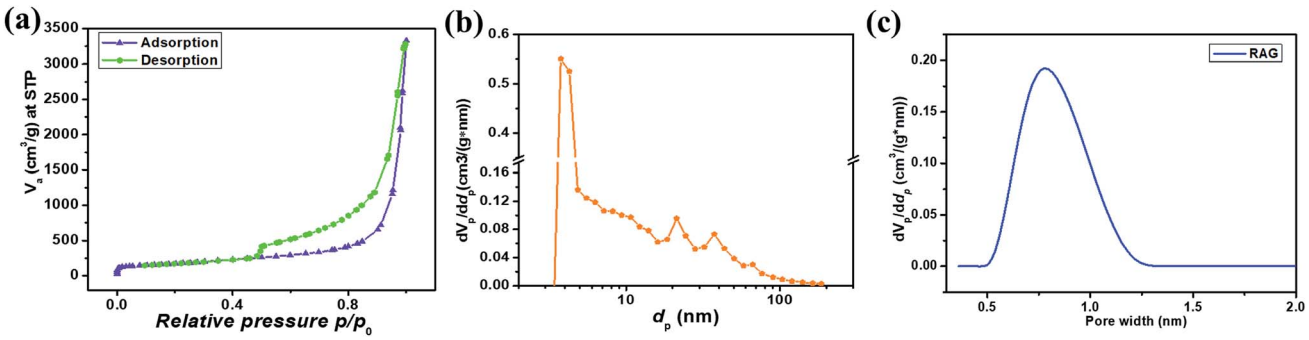

Fig. 3 (a) Nitrogen adsorption/desorption plot at 77.4 K for the RAG sample. (b) BJH pore-size distribution of RAG in mesopore and macropore regimes. (c) NLDFT pore size distribution of RAG in the micropore regime.

charged/discharged with physical ion migration rather than the pseudocapacitive reactions. The marginal current response in CV scans is due to the impact from the electrolyte, internal resistance, and scan rate.[60] The repeatability of the CV curves is attributed to the kinetic reversibility. Fig. 5b shows the GCD curve of the RAG supercapacitors with a constant current density from 1 A g^{-1} to 5 A g^{-1}. The initial voltage change of charging/discharging is due to the voltage drop in the internal resistance. Specific capacitances are extracted from GCD data at different current densities.[5,24,56,61] The specific capacitance of the RAG supercapacitor at the current density of 1 A g^{-1} is 279 F g^{-1}.[5,24,56,61] Increasing the current density to 2, 4, 5 and 7.5 A g^{-1}, the specific capacitance of the RAG supercapacitor decreases to 193, 139, 110, and 78 F g^{-1}, respectively. This specific capacitance compares favorably with the previously reported graphene materials. The curved graphene by hydrazine reduction demonstrated a specific capacitance of 154.1 F g^{-1} at 1 A g^{-1} with ionic liquid electrolyte;[22] a-MEGO by microwave radiation showed a gravimetric capacitance of 166 F g^{-1} in organic electrolyte,[61] laser-scribed graphene reached a specific capacitance of 276 F g^{-1} at a similar current density with ionic liquid electrolyte;[28] folded graphene prepared by pressing the graphene aerogel achieved a specific capacitance of 172 F g^{-1} at 1 A g^{-1} in $LiPF_6$ electrolyte.[62]

The Ragone plot in Fig. 5d reveals the energy storage performance of the RAG supercapacitor.

Energy densities are calculated based on the method demonstrated in previous reports.[5,24,56,61] The maximum energy density at 1 A g^{-1} is 135 W h kg^{-1}.[5,24,56,61] With an assumption that 30% weight of the device is from the RAG electrodes, the calculated systematical energy density is 40.5 W h kg^{-1}, which is still one order higher than those of the commercial supercapacitors (based on activated carbons).[63] The highest power density achieved at 7.5 A g^{-1} is around 7 kW kg^{-1}.

The RAG supercapacitor was further studied by impedance measurements in a frequency range from 1 MHz to 0.1 Hz. The Nyquist plot in Fig. 6 features a semi-circle in the high frequency region related to the resistive elements and a vertical spike in the low frequency region corresponding to the capacitive behavior of RAG supercapacitors. The ESR resistance at the *x*-intercept of the Nyquist plot is 4.4 ohm, suggesting a high charging/discharging rate in the RAG supercapacitors. The ion diffusion at the interface of the electrolyte and electrode lead to a short line with a nearly 45° slope, or Warburg resistance in the equivalent circuit of the supercapacitor. The very short Warburg

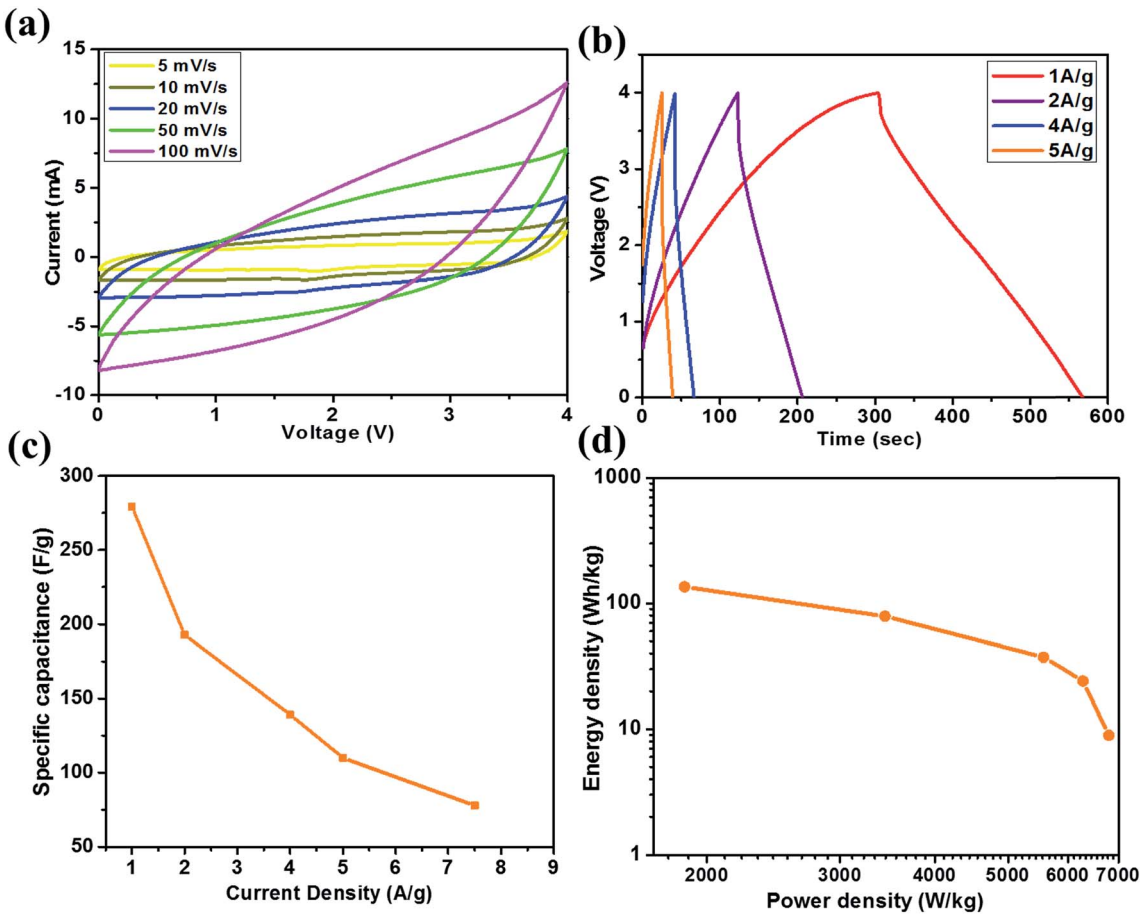

Fig. 5 (a) CV curves of the RAG electrode in $EMIMBF_4$ at different scan rates. (b) Galvanostatic charge–discharge curves of the supercapacitor in $EMIMBF_4$ for different current densities. (c) Specific capacitance *versus* current density for RAG supercapacitors. (d) Ragone plot of the developed RAG supercapacitors.

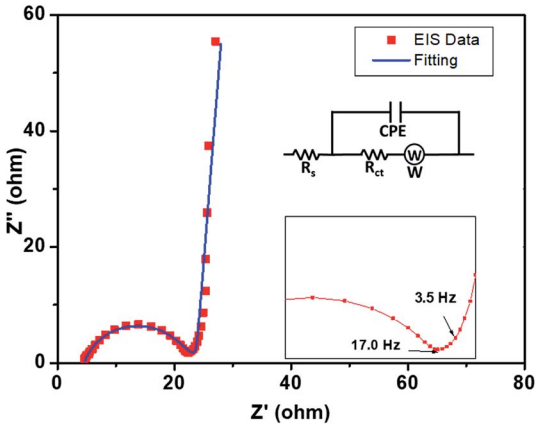

Fig. 6 Nyquist plot from EIS measurements. Inset shows the equivalent circuit for the EIS fitting.

line from 3.5 Hz to 17.0 Hz implies a short ion diffusion path, shown in the inset of Fig. 6.[63,64] By fitting the EIS data, a small Warburg impedance of 4 ohm and a high characteristic frequency of 10 rad s^{-1} are observed, which result in the short diffusion path in RAG electrodes.[65]

4. Conclusion

In summary, based on our experimental results, we can conclude that the rapid thermal annealing method produced high quality RAG for electrochemical energy storage applications. The prepared RAG materials show minimum oxygen content and form a graphitic material with the nanoporous morphology. The clear hexagonal electron diffraction spots suggest good crystallinity and minimum agglomeration in RAG materials. The small average interlayer spacing revealed by XRD and the high C/O ratio of 7.9 measured by XPS imply that RAG is well reduced during the thermal treatment. Compared with slowly annealed graphene, the RAG sample shows less oxygen content and better material quality. This work presents an effective strategy to produce high quality graphene materials and is suitable for mass production with a minimum environmental footprint. The symmetrical supercapacitors assembled with RAG electrodes deliver high specific capacitance and power density. They are capable of driving a wide variety of applications which demand high energy density and power density at low cost.

Conflicts of interest

There are no conflicts to declare.

Acknowledgements

This work is partially supported by the World Class University program (No. R31-10026) and National Research Foundation grant (No. 2017R1A2B3004049) funded by the Korean Ministry of Science, ICT and Future Planning.

References

1 M. Armand and J. M. Tarascon, Building better batteries, *Nature*, 2008, **451**, 652–657.
2 H. Wu, G. Yu, L. Pan, N. Liu, M. T. McDowell, Z. Bao and Y. Cui, *Nat. Commun.*, 2013, **4**, 1943.
3 C. M. Park, J. H. Kim, H. Kim and H. J. Sohn, *Chem. Soc. Rev.*, 2010, **39**, 3115–3141.
4 H. I. Becker, Low voltage electrolytic capacitor, *US. Pat.* 2800616A, 1957.
5 H. Yang, S. Kannappan, A. S. Pandian, J. H. Jang, Y. S. Lee and W. Lu, *J. Power Sources*, 2015, **284**, 146.
6 K. S. Novoselov, A. K. Geim, S. V. Morozov, D. Jiang, Y. Zhang, S. V. Dubonos, I. V. Grigorieva and A. A. Firsov, *Science*, 2004, **306**, 666–669.
7 K. S. Novoselov, A. K. Geim, S. V. Morozov, D. Jiang, M. I. Katsnelson, I. V. Grigorieva, S. V. Dubonos and A. A. Firsov, *Nature*, 2005, **438**, 197–200.
8 Y. Zhang, Y. W. Tan, H. L. Stormer and P. Kim, *Nature*, 2005, **438**, 201–204.
9 H. B. Heersche, P. Jarillo-Herrero, J. B. Oostinga, L. M. K. Vandersypen and A. F. Morpurgo, *Nature*, 2007, **446**, 56–59.
10 G. M. Rutter, J. N. Crain, N. P. Guisinger, T. Li, P. N. First and J. A. Stroscio, *Science*, 2007, **317**, 219–222.
11 N. Tombros, C. Jozsa, M. Popinciuc, H. T. Jonkman and B. J. van Wees, *Nature*, 2007, **448**, 571–574.
12 X. Fan, W. Peng, Y. Li, X. Li, S. Wang, G. Zhang and F. Zhang, *Adv. Mater.*, 2008, **20**, 4490–4493.
13 S. Stankovich, D. A. Dikin, G. H. B. Dommett, K. M. Kohlhaas, E. J. Zimney, E. A. Stach, R. D. Piner, S. T. Nguyen and R. S. Ruoff, *Nature*, 2006, **442**, 282–286.
14 D. A. Dikin, S. Stankovich, E. J. Zimney, R. D. Piner, G. H. B. Dommett, G. Evmenenko, S. T. Nguyen and R. S. Ruoff, *Nature*, 2007, **448**, 457–460.
15 X. Wang, Y. Zhang, C. Zhi, X. Wang, D. Tang, Y. Xu, Q. Weng, X. Jiang, M. Mitome, D. Golberg and Y. Bando, *Nat. Commun.*, 2013, **4**, 2905.
16 K. H. Kim, M. Yang, K. M. Cho, Y. Jun, S. B. Lee and H. Jung, *Sci. Rep.*, 2013, **3**, 3251.
17 L. Zhang, F. Zhang, X. Yang, G. Long, Y. Wu, T. Zhang, K. Leng, Y. Huang, Y. Ma, A. Yu and Y. Chen, *Sci. Rep.*, 2013, **3**, 1408.
18 H. Park, J. A. Rowehl, K. K. Kim, V. Bulovic and J. Kong, *Nanotechnology*, 2010, **21**, 505204.
19 V. Tozzini and V. Pellegrini, *Phys. Chem. Chem. Phys.*, 2013, **15**, 80.
20 S. P. Surwade, S. N. Smirnov, I. V. Vlassiouk, R. R. Unocic, G. M. Veith, S. Dai and S. M. Mahurin, *Nat. Nanotechnol.*, 2015, **10**, 459.
21 Z. Yan, G. Liu, J. M. Khan and A. A. Balandin, *Nat. Commun.*, 2012, **3**, 827.
22 C. Liu, Z. Yu, D. Neff, A. Zhamu and B. Z. Jang, *Nano Lett.*, 2010, **10**, 4863.
23 S. Park and R. S. Ruoff, *Nat. Nanotechnol.*, 2009, **4**, 217.

24 Y. Zhu, S. Murali, M. D. Stoller, A. Velamakanni, R. D. Piner and R. S. Ruoff, *Carbon*, 2010, **48**, 2118.
25 H. C. Schniepp, J. Li, M. J. McAllister, H. Sai, M. Herrera-Alonso, D. H. Adamson, R. K. Prud'homme, R. Car, D. A. Saville and I. A. Aksay, *J. Phys. Chem. B*, 2006, **110**, 8535.
26 M. Jin, T. H. Kim, S. C. Lim, D. L. Duong, H. J. Shin, Y. W. Jo, H. K. Jeong, J. Chang, S. Xie and Y. H. Lee, *Adv. Funct. Mater*, 2011, **21**, 3496.
27 S. Stankovicha, D. A. Dikina, R. D. Pinera, K. A. Kohlhaasa, A. Kleinhammesc, Y. Jiac, Y. Wuc, S. T. Nguyenb and R. S. Ruoff, *Carbon*, 2007, **45**, 1558.
28 M. F. El-Kady, V. Strong, S. Dubin and R. B. Kaner, *Science*, 2012, **335**, 1326.
29 Y. Zhu, S. Murali, W. Cai, X. Li, J. W. Suk, J. R. Potts and R. S. Ruoff, *Adv. Mater.*, 2010, **22**, 3906–3924.
30 C. Xue, M. Gao, Y. Xue, L. Zhu, L. Dai, A. Urbas and Q. Li, *J. Phys. Chem. C*, 2014, **118**, 15332–15338.
31 L. Wang, H. K. Bisoyi, Z. Zheng, K. G. Gutierrez-Cuevas, G. Singh, S. Kumar, T. J. Bunning and Q. Li, *Mater. Today*, 2017, **20**, 230–237.
32 W. Z. Bao, F. Miao, Z. cheng, H. Zhang, W. Y. Jang, C. Dames and C. N. Lau, *Nat. Nanotechnol.*, 2009, **4**, 562–566.
33 G. Peng, H. Song and X. H. Chen, *Electrochem. Commun.*, 2009, **11**, 1320–1324.
34 M. J. McAllister, J. L. Li, D. H. Adamson, H. C. Schniepp, A. A. Abdala, J. Liu, M. H. Alonso, D. I. Milius, R. Car, R. K. Prud'homme and I. A. Aksay, *Chem. Mater.*, 2007, **19**, 4396–4404.
35 Q. Du, M. Zheng, L. Zhang, Y. Wang, J. Chen, L. Xue, W. dai, G. Ji and J. Cao, *Electrochim. Acta*, 2010, **55**, 3897–3903.
36 B. Zhao, P. Liu, Y. Jiang, D. Pan, H. Tao, J. Song, T. Fang and W. Xu, *J. Power Sources*, 2012, **198**, 423–427.
37 N. I. Kovtyukhova, P. J. Ollivier, B. R. Martin, T. E. Mallouk, S. A. Chizhik, E. V. Buzaneva and A. D. Gorchinskiy, *Chem. Mater.*, 1999, **11**, 771–778.
38 J. D. Bernal, *Proc. R. Soc. London, Ser. A*, 1924, **106**, 749–773.
39 Y. Baskin and L. Meyer, *Phys. Rev.*, 1955, **100**, 544.
40 D. Chung, *J. Mater. Sci.*, 2002, **37**, 1475–1489.
41 A. C. Ferrari and J. Robertson, *Phys. Rev. B: Condens. Matter Mater. Phys.*, 2000, **61**, 14095.
42 K. N. Kudin, B. Ozbas, H. C. Schniepp, R. K. Prud'homme, I. A. Aksay and R. Car, *Nano Lett.*, 2008, **8**, 36–41.
43 G. D. Lee, C. Z. Wang, E. Yoon, N. M. Hwang, D. Y. Kim and K. M. Ho, *Phys. Rev. Lett.*, 2005, **95**, 205501.
44 A. J. Stone and D. J. Wales, *Chem. Phys. Lett.*, 1986, **128**, 501–503.
45 F. Tuinstra and J. L. Koenig, *J. Chem. Phys.*, 1970, **53**, 1126.
46 T. Livneh, T. L. Haslett and M. Moskovits, *Phys. Rev. B: Condens. Matter Mater. Phys.*, 2002, **66**, 195110.
47 L. G. Cançado, M. A. Pimenta, B. R. A. Neves, M. S. S. Dantas and A. Jorio, *Phys. Rev. Lett.*, 2004, **93**, 247401.
48 D. Graf, F. Molitor, K. Ensslin, C. Stampfer, A. Jungen, C. Hierold and L. Wirtz, *Nano Lett.*, 2007, **7**, 238–242.
49 C. Kozlowski and P. M. A. Sherwood, *J. Chem. Soc., Faraday Trans. 1*, 1984, **80**, 2099–2107.
50 M. Naebe, J. Wang, A. Amini, H. Khayyam, N. Hameed, L. H. Li, Y. Chen and B. Fox, *Sci. Rep.*, 2014, **4**, 4375.
51 L. Shahriary and A. A. Athawale, *Int. J. Renew. Energy Environ. Eng.*, 2014, **2**, 58–63.
52 S. Mohammadi, F. Afshar Taromi, H. Shariatpanahi, J. Neshati and M. Hemmati, *J. Ind. Eng. Chem.*, 2014, **20**, 4124–4139.
53 L. C. O. Silva, G. G. Silva, P. M. Ajayan and B. G. Soares, *J. Mater. Sci.*, 2015, **50**, 6407–6419.
54 H. Guo, X. Wang, Q. Qian, F. Wang and X. Xia, *ACS Nano*, 2009, **3**, 2653–2659.
55 K. S. W. Sing, D. H. Everett, R. A. W. Haul, L. Moscou, R. A. Pierotti, J. Rouquerol and T. Siemeniewska, *Pure Appl. Chem.*, 1985, **57**, 603–619.
56 H. Yang, S. Kannappan, A. S. Pandian, J. Jang, Y. S. Lee and W. Lu, *Nanotechnology*, 2017, **28**, 445401.
57 S. Some, Y. Kim, E. Hwang, H. Yoo and H. Lee, *Chem. Commun.*, 2012, **48**, 7732–7734.
58 R. F. Rajter, R. H. French, W. Y. Ching, W. C. Carter and Y. M. Chiang, *J. Appl. Phys.*, 2007, **101**, 054303.
59 Sigma Aldrich Chem Files, Ionic Liquids, Vol. 5, No. 6, web-accessed at http://www.sigmaaldrich.com/content/dam/sigma-aldrich/docs/Aldrich/Brochure/al_chemfile_v5_n6.pdf.
60 J. Jiang and A. Kucernak, *Electrochim. Acta*, 2002, **47**, 2381–2386.
61 Y. Zhu, S. Murali, M. D. Stoller, K. J. Ganesh, W. Cai, P. J. Ferreira, A. Pirkle, R. M. Wallace, K. A. Cychosz, M. Thommes, D. Su, E. A. Stach and R. S. Ruoff, *Science*, 2011, **332**, 1537–1541.
62 F. Liu, S. Song, D. Xue and H. Zhang, *Adv. Mater.*, 2012, **24**, 1089–1094.
63 B. E. Conway, *Electrochemical Supercapacitors: Scientific Fundamentals and Technological Applications*, Kluwer Academic/Plenum Publishers, New York, 1999.
64 Y. Wang, Z. Shi, Y. Huang, Y. Ma, C. Wang, M. Chen and Y. Chen, *J. Phys. Chem. C*, 2009, **113**, 13103.
65 J. Bisquert, G. Garcia-Belmontea, P. Buenob, E. Longob and L. O. SBulhõesb, *J. Electroanal. Chem.*, 1998, **452**, 229–234.

